WELDING RESEARCH

SUPPLEMENT TO THE *WELDING JOURNAL*, NOVEMBER 2023
Sponsored by the American Welding Society

Impact of Plate Thickness and Joint Geometry on Residual Stresses in 347H Stainless Steel Welds

3D finite element models were used to investigate factors that can reduce stress relaxation cracking

BY Y. HONG, T. PICKLE, J. VIDAL, C. AUGUSTINE, AND Z. YU

Abstract

Weldments of 347H stainless steel are potentially susceptible to stress relaxation cracking at elevated service temperatures. Mitigation of stress relaxation cracking susceptibility within a multipass weld requires a good understanding of welding practices and manufacturing techniques to control high tensile residual stresses. In this work, the dependence of residual stress distribution in 347H stainless steel on base plate thickness, joint geometry design, and preheating condition was systematically investigated by using three-dimensional finite element models. The finite element models were validated through good agreement between neutron diffraction measurements and calculated elastic strains. The single-V-groove welds with and without a preheating step all produced similar peak von Mises residual stresses, above 450 MPa, within both the fusion zone and heat-affected zone (HAZ). In plates thicker than 0.5 in. (12.7 mm), high tensile residual stress could be observed in a relatively large area, from the middle of the plate thickness to underneath the top surface. A double-V groove shifted the high tensile stress area to the middle thickness of the weld. A single-J-groove weld was able to confine the residual stress to a very small region near the middle thickness within the fusion zone and suppressed the von Mises residual stress within the HAZ to below 400 MPa.

Keywords

- Finite Element Modeling
- Welding
- Residual Stress
- Stainless Steel

https://doi.org/10.29391/2023.102.021

Introduction

Most advanced and reliable concentrating solar power systems integrated with a conventional steam Rankine power cycle use two-tank molten salt thermal energy storage (TES). This combination offers the opportunity to make these plants economically competitive and reliable when producing green electricity. These molten nitrate salt TES tanks are of considerable interest because they allow for electricity generation when the sun is not shining, increasing the plant capacity factor, utilization of capital equipment, and total annual generation while reducing energy costs (Ref. 1).

Due to the nature of the molten salt, the temperatures in the hot tanks go up to 565°C (1050°F) during service. High-temperature molten salts pose a potential corrosion issue in hot tanks. Type 347H stainless steel (SS) has been widely used in these hot tanks (Ref. 2). 347H is stabilized by the addition of strong carbide-forming elements (e.g., Nb), which not only reduces sensitization associated with the formation of chromium carbide at elevated service temperatures in other 300 series SS grades (e.g., 304H) but also improves creep strength and the maximum allowable work stress (Refs. 3–5). However, several types of failures were reported in 347H SS and its weldments, including liquation cracking (Refs. 6–9), ductility-dip cracking (Refs. 10–13), and reheat cracking or stress relaxation cracking (SRC) (Refs. 10, 12, 14–18). Among these types of failures, SRC is a very common failure mechanism for precipitation-strengthened SS welds at elevated service temperatures without prior stress relief. SRC is manifested in the form of high-temperature intergranular cracking largely due to grain-boundary (GB) creep associated with high welding-induced residual stresses, the elevated service temperature, and susceptible microstructures. The susceptible microstructures include precipitate-free zones formed adjacent to GBs within the coarse-grained heat-affected zone (HAZ) associated with reprecipitation of Nb(C,N) (Refs. 19, 20), sigma-phase formation along GBs within the weld metal (Refs. 21, 22), and excessive cellular Nb(C,N) eutectic phases

forming at GBs within the partially melted zone (PMZ) (Refs. 6, 9).

Worldwide, more than 50 SRC issues have been reported for austenitic steels (including 347H, 304H, 316H, 310, and 321H) on base and weld metals, particularly in the HAZ when operating over long periods above 500°C (932°F). The commonality of these failures is that in most of the fabrications, postweld heat treatment was not performed (Ref. 1). It is known that weld fabrication for 347H SS and other austenitic SS grades incur significant amounts of residual stress, especially for thick sections (e.g., 2 in. [50.8 mm] for commercial concentrating solar power TES hot tanks), due to mechanical constraint and high coefficients of thermal expansion during weld thermal cycles. Therefore, it is critical to understand the dependence of residual stress distribution in 347H SS on base plate thickness, joint geometry design (e.g., joint type and groove angle), and welding parameters (including heat input, number of weld passes, welding sequence, external mechanical constraints, and preheating, among others). Experimentally, residual stresses can be measured destructively or nondestructively. For instance, sectioning (Refs. 23, 24), hole-drilling (Ref. 25), and contour (Ref. 26) methods were employed to measure stresses destructively. Nondestructive measurements of residual stress include x-ray diffraction and neutron diffraction techniques (Refs. 27–32) and an ultrasonic method (Refs. 33, 34). Neutron diffraction is a powerful method that enables three-dimensional (3D) mapping of stress distribution in relatively thick steel plates (e.g., tens of centimeters) with a submillimeter spatial resolution.

Many modeling efforts and literature reviews have been made in the past few decades for simulation of weld-induced residual stresses using empirical, semiempirical, and process simulation methods (Refs. 35–40). Among those, thermo-mechanical-metallurgical simulation is considered as the basic but most accurate process simulation method that predicts the entire physical process of welding (Refs. 40–42). In this study, to reveal the impact of welding conditions on residual stress distribution in 347H SS plates, the thermo-elastic-plastic method was utilized for residual stress simulation while ignoring the metallurgical factors (i.e., solid-state phase transformation behavior) since the plate was an austenitic SS grade. Specifically, a sequentially coupled thermal and mechanical finite element (FE) model was established to evaluate the impact of plate thickness, joint geometry, and preheating condition on residual stress evolution within the 347H plates. The welding heat source can be described by either surface or volumetric distribution functions, which depend on welding processes. Goldak's double-ellipsoidal model (Ref. 42) is a nonaxisymmetric 3D model that simulates a complex liquid metal pool. It is currently widely used for simulating fusion welding processes, including gas tungsten arc welding (GTAW), gas metal arc welding, submerged arc welding (Ref. 43), and flux cored arc welding (Refs. 44, 45). Hence, in this work, Goldak's heat source model was utilized in the heat transfer analysis, which then served as an input for the mechanical model. The simulation results were compared to neutron diffraction measurement results for validation. By combining the FE simulation results generated from this work with experimental thermomechanical reheat crack susceptibility tests (details can be found in Ref. 46), a fundamental understanding of the susceptibility of 347H SS to SRC as a function of temperature, stress, and microstructure was achieved and serves as critical information to guide SRC mitigation solutions.

Methodology

The 347H SS welds in TES hot tanks were duplicated in the lab by adopting the actual welding parameters specified in welding procedure specifications and the corresponding prequalification records from the fabrication of current state-of-the-art concentrating solar power/TES commercial tanks. Two base plates 6 in. wide and 12 in. long (152.4 × 304.8 mm) with a thickness of 2 in. were welded by filling a single-V, 50 deg, 1/8-in. (~3.2 mm) root opening groove with 40 passes. The welding wire used was E347. GTAW was used for an open root pass (with 140 A, 11.5 V, and 5.45-min weld time) and a subsequent weld pass (165 A, 12.5 V, and 4.67-min weld time) while shielding the back surface of the weld with argon. Shielded metal arc welding (SMAW) was used for the remaining intermediate weld passes with 155 A, 23 V, and weld times ranging from 2.40 to 4.67 min. The SMAW procedure used a high deposition rate and, thus, slow travel speeds (the minimum allowed by the welding procedure specifications) along with a weaving technique according to AWS D1.6, *Structural Welding Code — Stainless Steel*, Section 3.29 (Ref. 47), to achieve maximum deposition while using the minimum number of passes for the specific single-V geometry. The diameter of the electrode used for all SMAW was 5/32 in. (~4.0 mm), whereas the GTAW wires were 3/32 in. (~2.4 mm) in diameter. The parameters for each welding pass, including the mean current, voltage, weld time, weld length, and calculated travel speed serving as the input parameters for the FE model to calculate the corresponding heat inputs, are tabulated in Table 1. Note that the travel speeds and, thus, weld times varied among passes 3–40 in the actual welding experiment since they were manually controlled to ensure sufficient deposition. The interpass temperatures were maintained at 80°C (176°F), which included roughly a 20-min cool time after the completion of each pass prior to each successive pass. The Abaqus software was used to build the model.

Figure 1 illustrates the pass sequence and joint geometry of the duplicate welds. As illustrated in Fig. 1, the mesh size gradually increased from the weld centerline to the edge of the plate to ensure that sufficient details of the thermo-mechanical profile were captured in the weld area while minimizing computation time. Convergence analysis was performed to confirm the accuracy of the analysis, and the minimum element size required was determined to be 0.5 mm (0.020 in.). For the 2-in., 40-pass, single-V weld, there were a total of 72,160 elements with an 8-node linear brick type. The numbers in Fig. 1B represent the weld pass number as the material was deposited into the weld. The meshes of each weld pass were deactivated initially in the FE model and were then activated one by one, simulating filler metal deposition.

To reveal the effects of joint geometry, plate thickness, and preheating on residual stress distribution in 347H SS welds, six models were analyzed. This included varying the plate

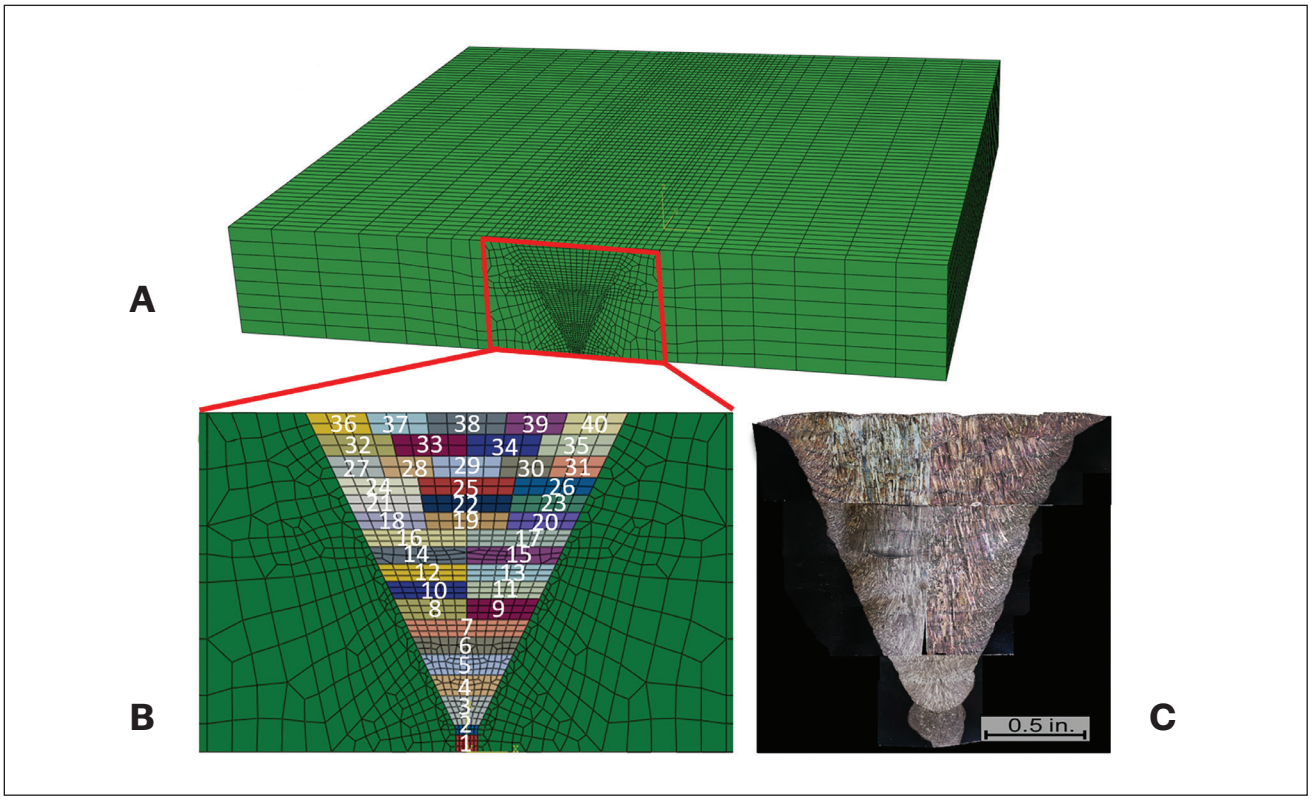

Fig. 1 — A — Finite element model (FEM) mesh of the 12 × 12-in. plate; B — meshes of the weld zone with different colors representing the element sets of each weld pass; C — cross-sectional macrograph of the weld zone.

Table 1 — Welding Parameters Applied in Abaqus Simulation*

Pass #	Process	Mean Current (A)	Mean Volts (V)	Weld Time (min)	Weld Length (in.)	Avg. Travel Speed (in./min)
1	GTAW	140	11.5	5.45	14	2.57
2	GTAW	165	12.5	4.67	14	3.00
3-40	SMAW	155	23	2.40–4.33	14	3.02–5.83

***2-in. plate with 40 weld passes**

thickness from 2 in. to 1 in. (25.4 mm) and 0.5 in., replacing the single-V groove with a double-V and single-J groove in the 1-in.-thick plate, and, lastly, preheating to 232°C (450°F) for 20 min on the 1-in.-thick plate. The weld sequence, which went from left to right for each weld layer, was the same for all the single-V and single-J groove welds. By reducing the plate thickness, the total number of weld passes for the single-V groove reduced from 40 passes for the 2-in. plate to 16 passes for the 1-in. plate and six passes for the 0.5-in. plate. In comparison, eight weld passes were used to fill the single-J groove joint in the 1-in.-thick plate with a groove radius of 4.2 mm (0.165 in.) and bevel angle of 33.44 deg.

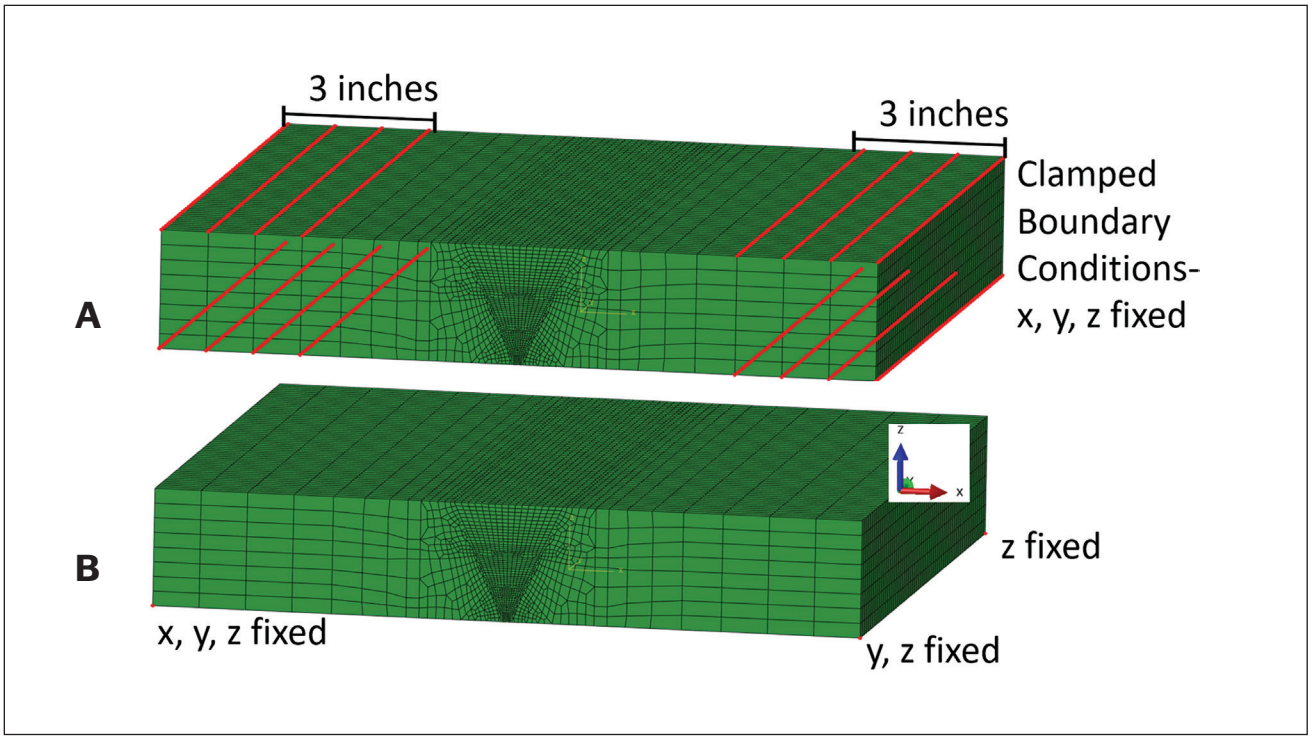

Fig. 2 — Boundary conditions for clamped (A) and unclamped (B) conditions of the weld model.

Welding in the double-V-groove joint was carried out in an oscillating sequence — one layer on one side was welded (left to right) first followed by a layer with the same weld pass progressions on the opposite side until the joint was complete. A total of nine layers and 11 passes were set up in the double-V-groove weld model.

As shown in Fig. 2, two sequential boundary conditions — clamped and unclamped — were applied to the welds after welding completion, simulating actual lab welding procedures. In the clamped boundary condition, each side of the weld had x, y, and z fixed within an area that was approximately 3 in. (76.2 mm) wide, as shown in Fig. 2A. This boundary condition was maintained for the duration of the welding procedure. After completion of the weld process and cooling to room temperature, the model was unclamped by fixing x, y, and z motion on one corner and fixing y, z motion and z motion, respectively, for the two corners on the other side of the weld, as illustrated in Fig. 2B.

In the weld models, nonlinear transient heat conduction analysis was performed first to obtain the thermal profile associated with each welding pass with a thermal 8-node DC3D8 element. In the multipass welding model, only first-pass elements were activated during the first weld pass while the other pass elements were deactivated. After the first weld was finished, the elements for the second pass were activated, and so forth. The calculated thermal profile was employed as a thermal body load in the subsequent nonlinear mechanical elastic-plastic calculation to obtain the stress evolution with a C3D8R element. The clamped boundary condition was first activated during the welding procedure and was then deleted after cooling for 20 h to room temperature to calculate the stress redistribution.

The double-ellipsoidal heat source model developed by Goldak et al. (Ref. 48) was used to simulate the weld heat input, as illustrated in Fig. 3A. The front and rear of the heat flux are described by Equations 1 and 2, respectively:

$$q_r(x,y,z) = \frac{6\sqrt{3}f_r\eta Q}{a_r bc\pi\sqrt{\pi}} \exp\left(-\frac{3x^2}{a_r^2} - \frac{3y^2}{b^2} - \frac{3z^2}{c^2}\right) \quad (1)$$

$$q_f(x,y,z) = \frac{6\sqrt{3}f_f\eta Q}{a_f bc\pi\sqrt{\pi}} \exp\left(-\frac{3x^2}{a_f^2} - \frac{3y^2}{b^2} - \frac{3z^2}{c^2}\right) \quad (2)$$

where the front and rear quadrant fractions, f_f and f_r, were set as 0.6 and 1.4, respectively. The heat input was $Q = VI\eta$, where the arc efficiency (η) was set to be 0.8, and voltage (V) and current (I) were dependent on the pass number. a_f, a_r, b, and c were dependent on the specific pass number so that the predicted region of solidification pertained to the width and depth of the corresponding experimental pass, as illustrated by the macrograph in Fig. 1C. The travel rate of the heat source was dependent on the weld speed specific to each pass. The local coordinates were x, y, z, and the travel speed was considered into the calculation by defining y equal to y' + vt, where y' was the global coordinate , v was the travel speed, and t was the time during each pass. The interpass temperatures were maintained at the experimentally observed 80°C, which included roughly a 20-min cool time after the completion of each pass prior to each successive pass. Convective cooling was allowed with an ambient tem-

Table 2 — Temperature-Dependent Mechanical and Thermal Properties (Refs. 49, 50)

Temp. (°C)	Density (e-9 kg/mm³)	Specific Heat (e8 mJ/(K·kg))	Conductivity (mW/(mm·K))	Young's Modulus (GPa)	Expansion Coefficient (e-6)/s	Poisson's Ratio
20	7.9	4.43	15	200	16.5	0.278
100					17.5	
200	7.8	5.15	17.5	185	18	0.288
400	7.7	5.63	20	170	18.5	0.298
538				156		0.298
600	7.6	5.81	22.5	153	19	0.313
800	7.5	6.09	25.5	135	20	0.327
900	7.4				20	
1000		6.31	28.3	96	20.5	0.342
1100	7.3			70	21	0.342
1200		6.54	31.1	50	21	0.350
1300				10	22	0.351
1340		6.69	33.1			
1400		6.75			22.5	
1500	7.2				22.5	

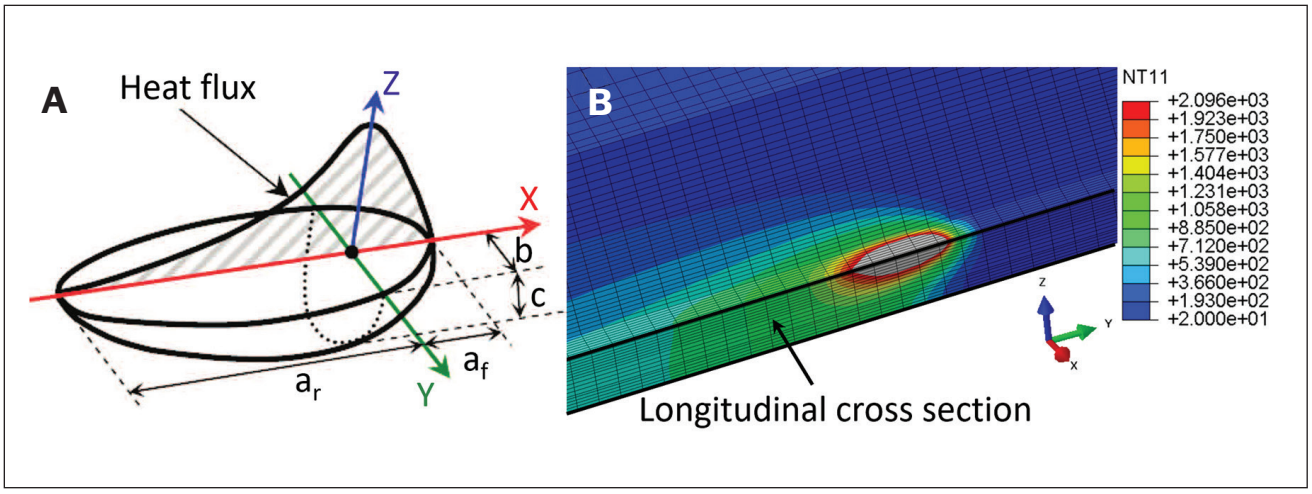

Fig. 3 — A — Goldak's heat source model (Ref. 48); B — an example temperature contour on a longitudinal cross section during the welding simulation of pass number 5.

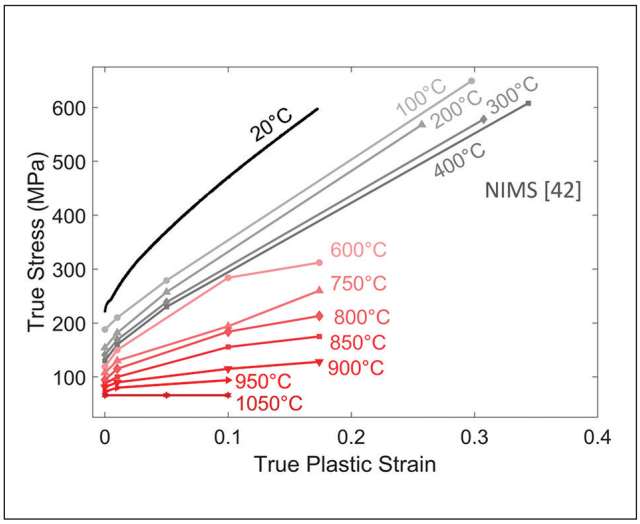

Fig. 4 — True stress-strain curves used in the materials database obtained from our thermomechanical testing using a Gleeble machine (Ref. 46) (in black and red) and NIMS data sheets (Ref. 51) (in gray).

perature boundary condition of 20°C (68°F). Figure 3B demonstrates an example of temperature distribution calculated at weld pass number 5 in the 2-in., 40-pass, single-V-groove weld model.

The temperature-dependent material properties, including density (Ref. 49), specific heat (Ref. 50), thermal conductivity (Ref. 50), Young's modulus (Ref. 50), Poisson's ratio (Ref. 50), and thermal expansion coefficient (Ref. 50), are tabulated in Table 2. Note that the material properties were assumed to be the same for both weldment and base metal because the weld model simulates the case with a matching filler metal, E347.

The temperature-dependent flow stress/strain data are summarized in Fig. 4. The data were extracted from our thermomechanical testing results using a Gleeble machine at room temperature (in black) and at 600°–1050°C (1112°–1922°F) (in red, details can be found in Ref. 46) and reference National Institute for Materials Science (NIMS) data sheets by Sawada et al. (Ref. 51) at 100°–400°C (212°–752°F) (in gray). Note that there was no strain hardening observed at 1050°C, which indicates there was no resistance to multiple cross slips at the early strain stage.

Results and Discussion

Thermal Profiles

The thermal profile calculation is demonstrated by a contour plot in Fig. 5A generated for pass number 31 of the 2-in.-thick, 40-pass, single-V-groove weld. Figure 5B shows a corresponding temperature profile at a cross section marked by the yellow block in Fig. 5A. Figure 5C compares the temperature profiles of three nodes, as highlighted in Fig. 5B, located within the weld metal with a peak temperature of 1843°C (3349°F), which is far beyond the liquidus temperature of 347H SS; the HAZ that experienced a peak temperature of 1354°C (2469°F); and the HAZ with a peak temperature of 774°C (1425°F). Ideally, temperature profiles recorded during welding would be the best approach for thermal model validation. Unfortunately, in this study, the thermal data was not available. Instead, the material's thermal and mechanical property inputs were validated through a Gleeble thermomechanical experiment, with the details to be published elsewhere.

Strain Profiles and Model Validation

The total strain calculated from the weld model was composed of the elastic, plastic, and thermal strain. Figure 6 summarizes and compares the elastic and plastic strain components of the total strain developed within the 2-in.-thick, single-V-groove 347H SS weld along three directions (where 11, 22, and 33 corresponded to x-, y-, and z-direc-

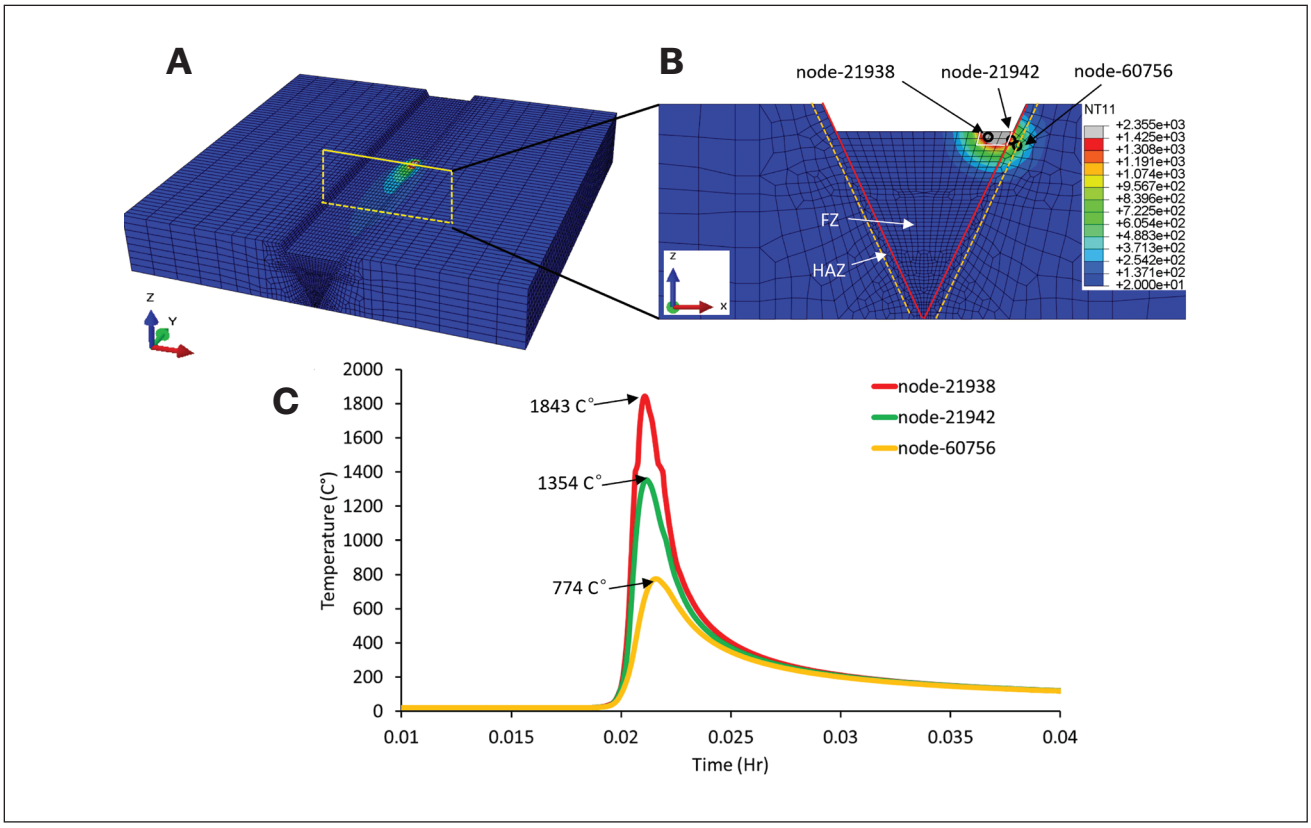

Fig. 5 — Temperature profiles experienced by the whole plate (A) and a cross-sectional view (B) and three nodes (C) as marked in B during pass 31 of the 2-in.-thick, 40-pass, single-V-groove weld.

tions, respectively) after welding completion, cooling to room temperature, and unclamping. The axes — x, y, and z — were parallel to the transverse direction (TD), longitudinal direction (LD), and normal direction (ND) of the welded plate, respectively. To be more specific, the y-axis was parallel to the welding direction. It can be observed that high tensile elastic strains evolved near the top center of the weld along the LD (//y), as shown in Fig. 6B, while high compressive elastic strain developed near the center of the weld along the TD (//x), as shown in Fig. 6A. High tensile elastic strain also developed near root/intermediate passes along the TD. Note that the unclamping step after welding introduced redistribution and relieving of elastic strain within the weld, as indicated by comparing the maximum elastic strain contour maps in Figs. 7A and B. On the contrary, there was no noticeable change in the plastic strain distributions along all three directions before and after unclamping, as demonstrated by the comparison of maximum principal plastic strain maps in Figs. 7C and D.

Comparing Figs. 6D–F to Fig. 7D reveals that plastic strains along the ND (//z) were the dominant components among the three directions. A maximum tensile plastic strain of approximately 21% developed near the root/intermediate passes of the 40-pass weld along the ND (//z). This high plastic strain near the joint root was induced by reheating and subsequent yielding during a multipass welding process and was observed to increase with an increasing number of weld passes. After seven passes, tensile plastic strain in the joint root did not further change because subsequent welds in the single-V groove moved sufficiently far away from the joint root. Adjacent to the boundary of the fusion zone (FZ) — within the PMZ and HAZ — the peak plastic strain was approximately 9% along the ND in the as-welded, unclamped condition, as shown in Fig. 6F. As discussed in the introduction, the FZ, PMZ, and HAZ of 347H SS welds often contain detrimental microstructural features. The presence of high tensile plastic strains within these susceptible locations would accelerate the initiation of microvoids and the formation of cracks and, thus, augment the susceptibility to SRC.

Neutron diffraction mapping of residual strains in the 2-in.-thick, 40-pass, single-V-groove weld was performed for the purpose of validating the weld model. Because of the nature of the neutron diffraction method, only elastic strains can be calculated. Details of the neutron diffraction measurement setup and data analysis can be found in Ref. 46. Note that because of the penetration limitation of neutrons within the 2-in.-thick 347H SS plate, the diffraction profile for elastic strain along the TD (parallel to the x, or 11, direction in Fig. 8A) was the only result demonstrating a high signal-to-noise ratio due to a relatively large allowable gauge volume of a 7.5 × 7.5 mm (0.295 × 0.295 in.) area on the transverse cross section (as marked out by the yellow dotted block in Fig. 8A) and 28 mm (1.102 in.) along the welding direction (parallel to the y-axis) during measurement. Three lines across the weld along the TD were mapped: one near the top surface (z = 11.5 mm [0.453 in.]), one at midthickness (z = 0 mm), and the last at the root of the weld (z = –20 mm [0.787 in.]), as marked in the elastic strain contour plot in Fig. 8A. Figure 8B compares the elastic strain profiles of (311) planes along the three lines

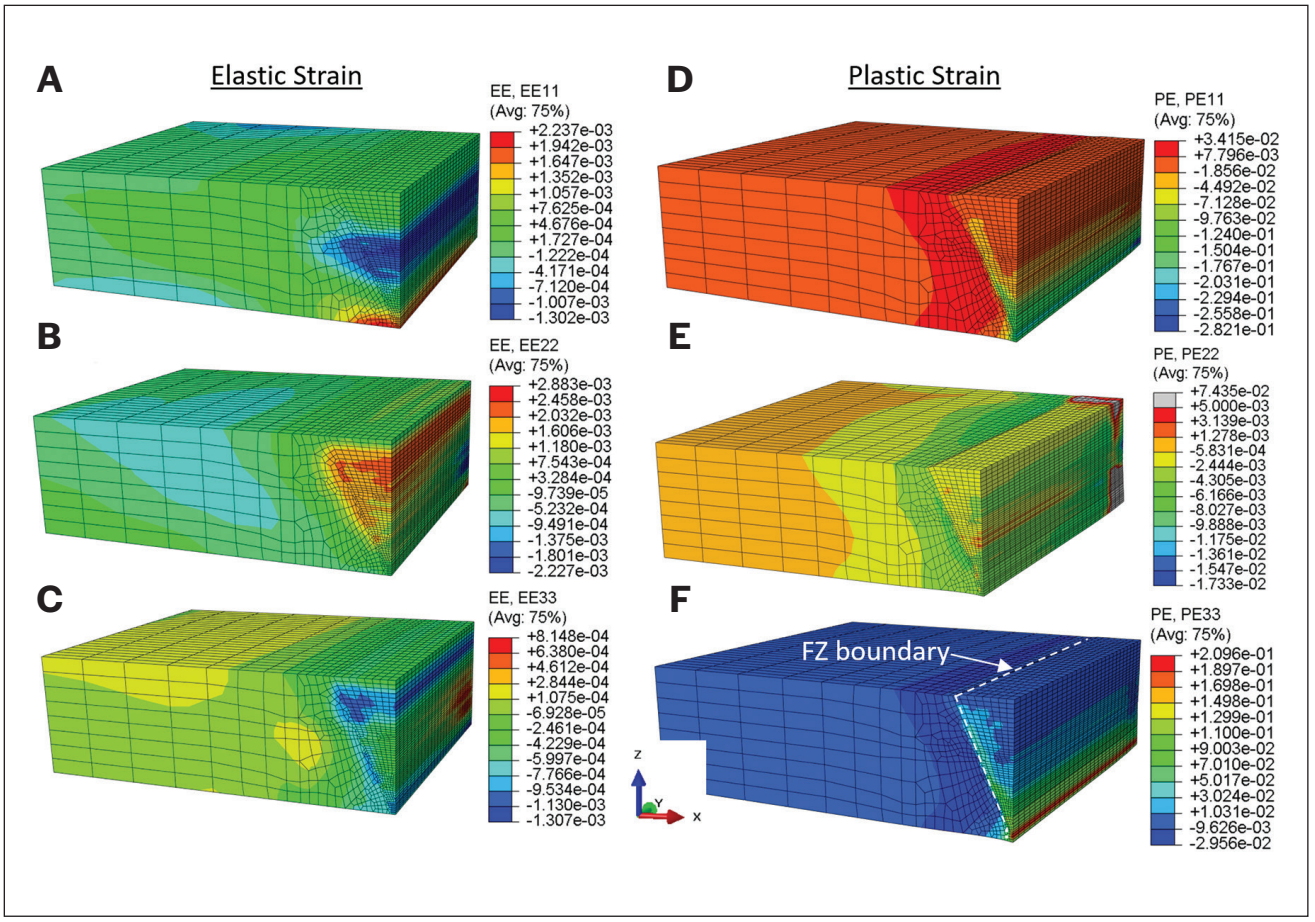

Fig. 6 — Elastic (A–C) and plastic (D–F) strain contours from finite element calculations along the transverse (//11), longitudinal (//22), and normal (//33) directions in the 2-in.-thick, single-V-groove weld (rear left quarter of the weld model). The x (i.e., 11), y (i.e., 22), and z (i.e., 33) axes represent transverse, longitudinal, and normal directions, respectively. FZ denotes fusion zone.

from neutron diffraction mapping to the bulk elastic strain calculated from the FE model. It should be noted that at each mapping point, the neutron diffraction result represents an averaged value from a relatively large diffraction volume, leading to an expected discrepancy between experimental and simulation results. In addition, the complex dilution and phase transformation behavior within the multipass weld region and HAZ lead to difficulty in accurate mapping of stress-free reference d spacing and, therefore, introduce additional uncertainty for strain and stress calculations from neutron diffraction experiments for welding applications. With all the above-mentioned factors influencing the neutron diffraction results and data analysis, a reasonable agreement was still reached on the overall trend of strain distributions between the FE analysis and the neutron diffraction results, with peak tensile strains near the joint root and compressive strains in midthickness. This good agreement validates the parameters used in the weld model and, therefore, the subsequent stress analysis.

Stress Profiles of All Cases

The SRC mechanism could be expedited by an excessive amount of stress and plastic deformation beyond the material's yield point that exhausts the maximum allowable creep strain at elevated temperatures. Therefore, instead of evaluating the maximum principal stresses, von Mises stress as an evaluation criterion for yielding was calculated for all the welded cases. The von Mises stress equation (Equation 3), which accounts for an effective combination of six stress components (σ_{ij}), is expressed as the following:

$$\sigma_{eff} = \left[\frac{(\sigma_{11} - \sigma_{22})^2 + (\sigma_{22} - \sigma_{33})^2 + (\sigma_{33} - \sigma_{11})^2}{2} + 3(\sigma_{12}^2 + \sigma_{13}^2 + \sigma_{23}^2) \right]^{1/2} \quad (3)$$

Figure 9 summarizes and compares stress contours for the TD (//11), LD (//22), and ND (//33) and the von Mises stress within the rear left quarter of the weld model. The effect of unclamping was evidenced by a reduction in stresses within the 347H SS weld along all three directions, especially along

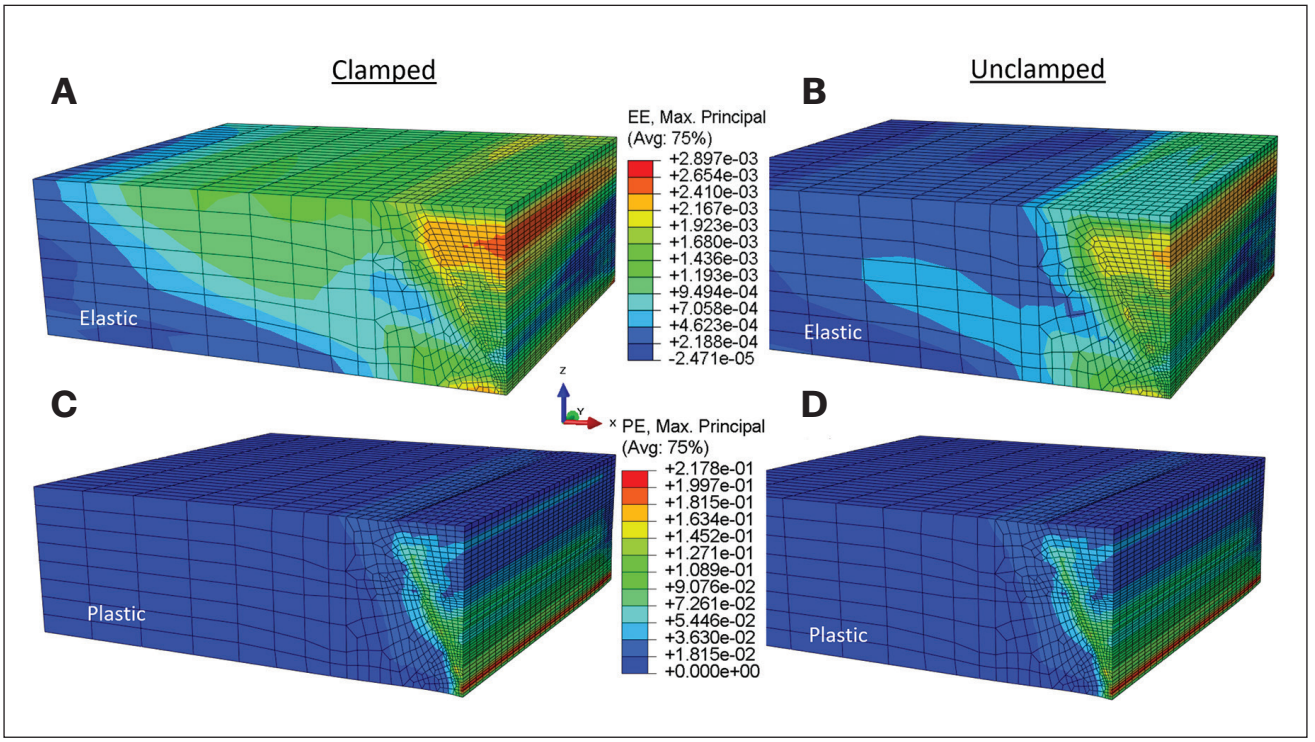

Fig. 7 — Comparison of the maximum principal elastic (A, B) and plastic (B, D) strain contours under clamped (A, C) and unclamped (B, D) conditions, where EE and PE represent elastic and plastic strain, respectively.

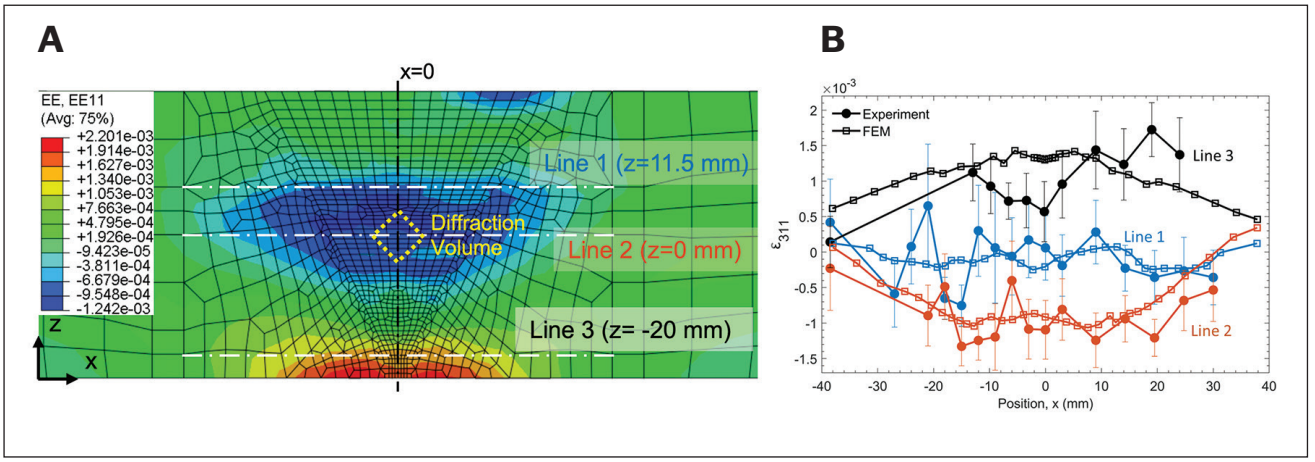

Fig. 8 — A — FEM of the TD elastic strain calculation in the 2-in.-thick, 40-pass weld after unclamping, with the three white dashed lines indicating the neutron diffraction mapping locations; B — comparison of elastic strain along the TD of (311) planes measured from neutron diffraction to FE-calculated bulk elastic strain. The yellow dotted block marks out the neutron diffraction volume.

the TD (//11) and LD (//22). For instance, in the 2-in.-thick, 40-pass, single-V-groove weld, von Mises stress above 550 MPa was observed near the top weld surface in the clamped condition (see Fig. 9A) and was reduced to below 500 MPa in the unclamped condition (see Fig. 9E). Along each direction after unclamping, high tensile stress (> 400 MPa) was observed in the root/intermediate pass along the TD and near the top surface along the LD. Low ND stress (< 66 MPa) developed throughout the weld, as shown in Fig. 9H.

The effect of plate thickness on residual stress distribution in single-V-groove 347 SS welds is demonstrated in Fig. 10. For both 2- and 1-in.-thick welds (Figs. 10A, B), high tensile residual stress (> 400 MPa) could be observed in a relatively large area, from middle plate thickness to underneath the top surface. The tensile stress in the 0.5-in. case in Fig. 10C exhibited a slightly lower peak value than the other two cases, but it was limited to a very small weld area near the middle thickness of the plate. Furthermore, the residual stress in the HAZ for the 0.5-in. case was much lower than that of the other

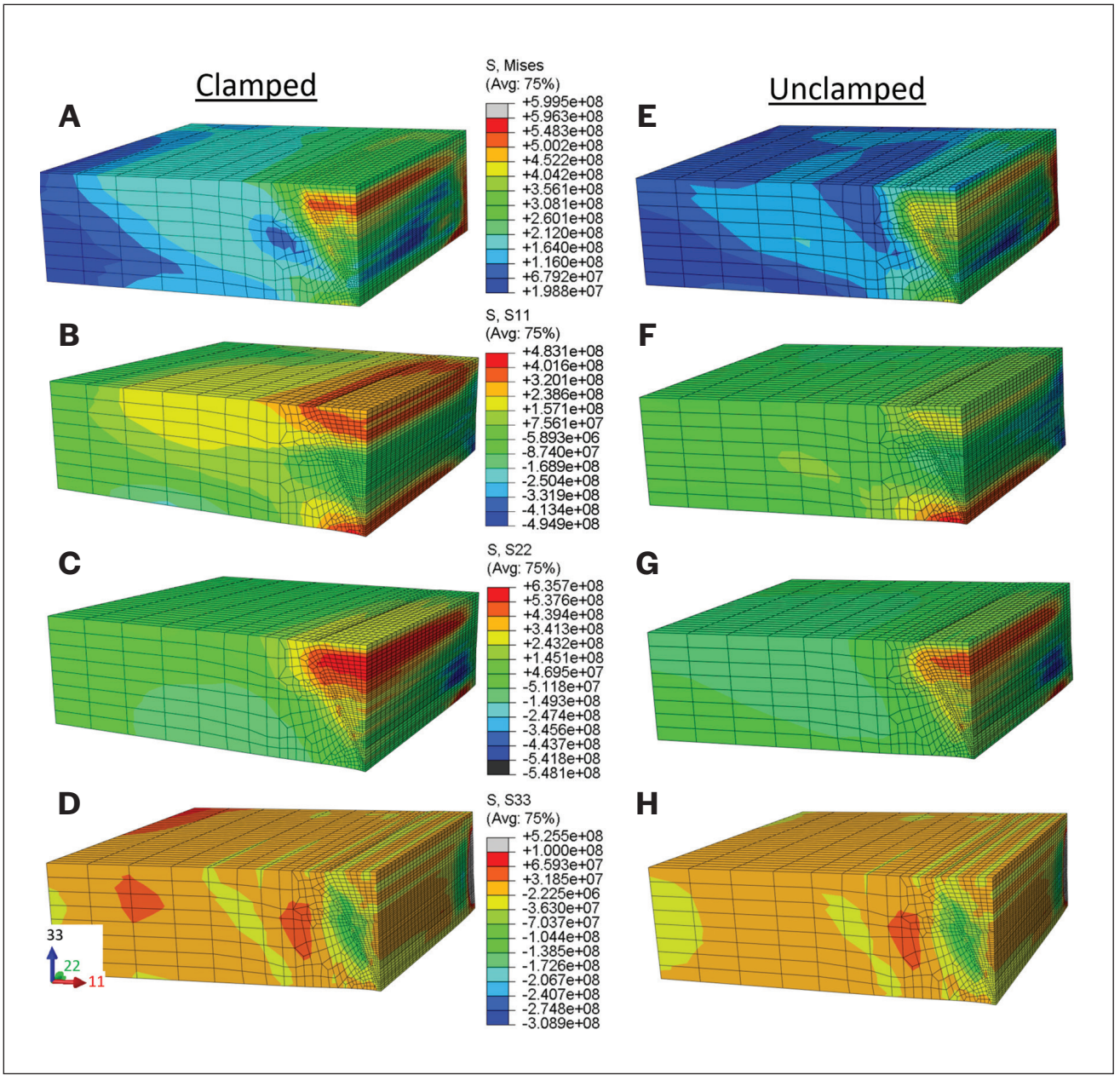

Fig. 9 — Contour maps of von Mises residual stress (Pa) (A) and transverse (B), longitudinal (C), and normal direction (D) stresses in clamped (A–D) and unclamped (E–H) conditions of the 2-in.-thick, single-V-groove 347H SS weld for the rear left quarter of the weld model.

two thicknesses. As mentioned in the introduction, the most susceptible microstructures for SRC include precipitate-free zones formed adjacent to GBs within the coarse-grained HAZ associated with reprecipitation of Nb(C,N) (Refs. 19, 20) and excessive cellular Nb(C,N) eutectic phases forming at GBs within the PMZ (Refs. 6, 9). Therefore, it is most concerning to observe high tensile residual stress within the HAZ. The modeling results suggest that 347H SS welds with a plate thickness lower than 0.5 in. have much lower susceptibility to reheat cracking or SRC due to the very limited high-stress-area size in the FZ and relatively low stress within the HAZ, which is attributed to fewer welding passes.

Figure 11A demonstrates the effect of a preheating step on the development of residual stress in the 1-in.-thick, single-V-groove weld. The base plate was preheated to 232°C for 20 min, which allowed for a uniform temperature distribution throughout the base plate. In comparison to Fig. 10B, the preheating process was able to confine the high residual stress to a very small area within the center of the 347H SS weld; however, it was not successful in controlling the residual stress in the HAZ. Hence, susceptibility to SRC within the HAZ, which is one of the most-often reported failure locations (Ref. 52), cannot be suppressed by using a preheating step alone. Replacing the filler metal E347 with a softer filler material with less susceptibility to SRC (e.g., E16.8.2) (Ref.

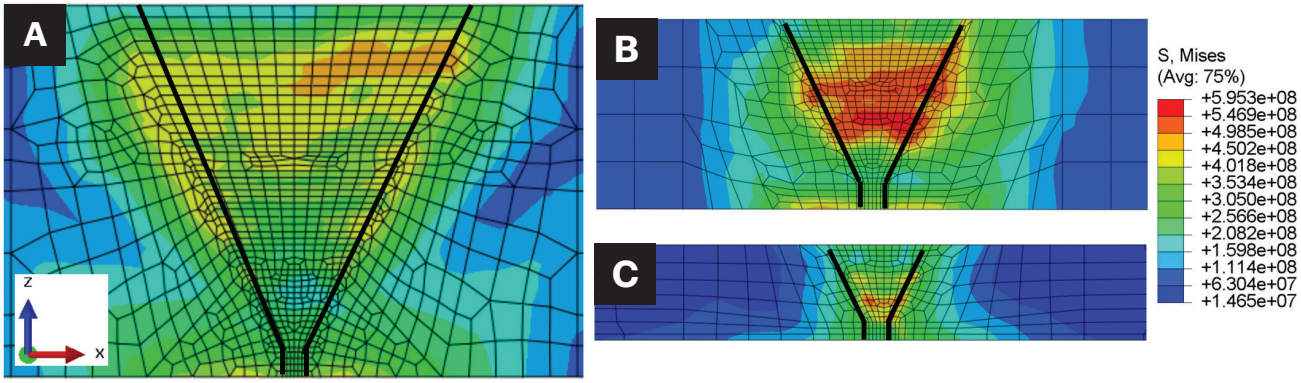

Fig. 10 — Cross-sectional view of stress contours in the middle of the weld length from single-V-groove welds with different base plate thicknesses: A — 2 in.; B — 1 in.; C — 0.5 in.

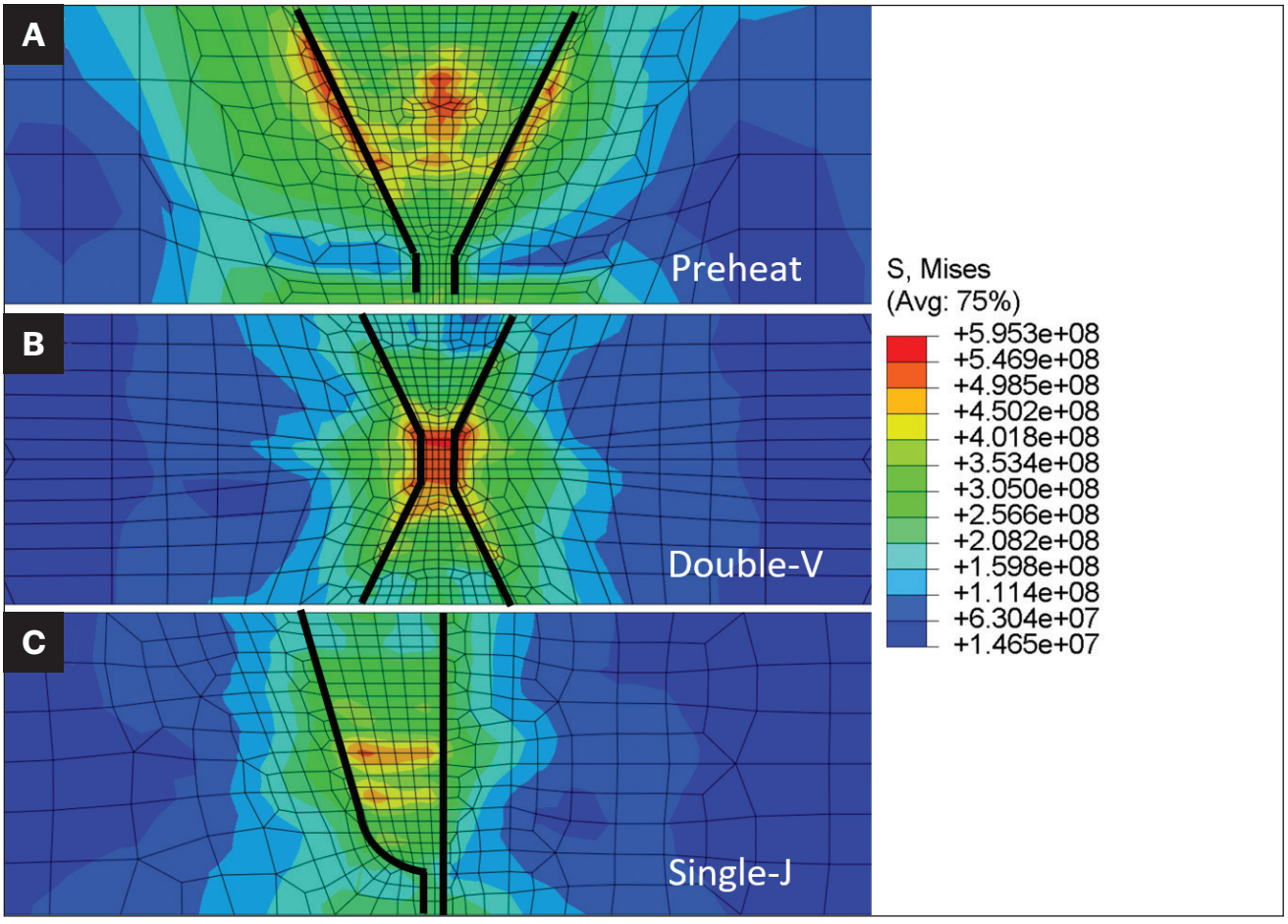

Fig. 11 — Cross-sectional view of stress contours in the middle of the weld length from 1-in.-thick welds with different reference temperatures and joint geometries: A — Single-V groove with preheating base plate to 232°C for 20 min; B — double-V groove without preheating; C — single-J groove without preheating.

33) in combination with a preheating process could serve as a potential solution for controlling residual stress in the HAZ because the soft filler material may deform more to allow for the relaxation of stress into neighboring regions.

By changing the joint geometry from single-V to double-V for the 1-in.-thick plate, as shown in Fig. 11B, the high-stress area is confined to a smaller area in the middle thickness of the welded plate while the peak stress value is still comparable to the single-V-groove joint. Finally, by changing the single-V groove to a J-bevel, as shown in Fig. 11C, the weld-induced peak residual stress is lower than in all other cases and also well controlled into a very small area near the

middle thickness of the weld. The peak HAZ residual stress in the J-groove case is also significantly lower than in the other cases. The reason for such an effective residual stress reduction is attributed to reducing the weld volume by nearly half in contrast to a single-V-groove joint. Therefore, weld geometry design plays a significant role in determining the residual stress distributions within a 347H SS weld. The joint geometry is dependent on the feasibility and versatility of the welding position. If feasible, a J-groove design is recommended for joints thicker than 0.5 in. in 347H SS welds for the purpose of reheating cracking or SRC control.

Conclusion

In summary, the effect of 347H SS plate thickness, joint geometry design, and preheating on residual stress distributions was investigated using 3D FE models. The following conclusions can be drawn:

The weld model predicted the elastic and plastic strain distributions before and after unclamping upon completion of a welding process. The unclamping step only impacted elastic strain redistribution. Good agreement was achieved between the elastic strains calculated from neutron diffraction measurements and FE modeling, thereby validating the weld models.

A comparison of the weld residual stress profiles generated for different base plate thicknesses showed that the 1- and 2-in. cases exhibited similar levels of peak residual stress within a relatively large area, while the 0.5-in. case showed slightly lower peak stress and a much more confined high-stress-area size.

The single-V-groove joint is not recommended for plates thicker than 0.5 in. due to the introduction of high residual stresses in the area from underneath the top surface to the middle thickness in both the FZ and HAZ, where high cracking susceptibility is expected.

In comparison to preheating and a double-V groove, the adoption of a J-bevel most effectively reduced residual stresses in the FZ and HAZ and, thus, is recommended for 347H SS joints greater than 0.5 in., if feasible, for field implementation.

Acknowledgments

This work was authored in part by the National Renewable Energy Laboratory, operated by Alliance for Sustainable Energy LLC for the U.S. Department of Energy (DOE) under Contract No. DE-AC36-08GO28308. Funding provided by U.S. DOE Office of Energy Efficiency and Renewable Energy, Solar Energy Technologies Office. The views expressed in the article do not necessarily represent the views of the DOE or the U.S. Government. The U.S. Government and the publisher, by accepting the article for publication, acknowledge that the U.S. Government retains a nonexclusive, paid-up, irrevocable, worldwide license to publish or reproduce the published form of this work, or allow others to do so, for U.S. Government purposes. This project is supported by the DOE under grant DE-EE00033458. The work benefited from Lincoln Electric and KISWEL Inc., which providing GTAW and SMAW consumables, and Brahma Group Inc., which provided guidance on welding procedures of the 2-in.-thick plate. We also acknowledge Dr. Wei Zhang for his constructive suggestion in building FE models. A portion of this research used resources at the High Flux Isotope Reactor, a DOE Office of Science User Facility operated by Oak Ridge National Laboratory (ORNL). We acknowledge Dr. Jeff Bunn, Dr. Andrew Payzant, and Paris Cornwell for their assistance with the high intensity diffractometer for residual stress analysis (HIDRA) beamline at ORNL.

References

1. Mehos, M., et al. 2017. Concentrating solar power Gen3 demonstration roadmap. Technical Report. National Renewable Energy Lab (NREL). *nrel.gov/docs/fy17osti/67464.pdf*

2. Thomas, R. D. 1984. HAZ cracking in thick sections of austenitic stainless steels — Part II. *Welding Journal* 63(12): 355-s to 368-s.

3. Abe, F., Kern, T.-U., and Viswanathan, R. 2008. *Creep-Resistant Steels*. Cambridge, England: Woodhead Publishing.

4. Sedriks, A. J. 1996. *Corrosion of Stainless Steel*, Second Edition. Hoboken, N.J.: John Wiley & Sons.

5. Khatak, H. S., and Raj, B., eds. 2002. *Corrosion of Austenitic Stainless Steels: Mechanism, Mitigation and Monitoring*. Cambridge, England: Woodhead Publishing.

6. Messler, R. W., and Li, L. 1997. Weld heat affected zone liquation cracking in type 347 stainless steel. *Science and Technology of Welding and Joining* 2(2): 10. DOI: 10.1179/stw.1997.2.2.43

7. Lundin, C. D., et al. 1988. Weldability evaluations of modified 316 and 347 austenitic stainless steels: Part 1 — Preliminary results. *Welding Journal* 67(2): 35-s to 46-s.

8. Lundin, C. D., et al. 1991. Weldability of nuclear grade stainless steels — Evaluation of HAZ cracking susceptibility of 347 nuclear grade stainless steels. *Proceedings of the International Conference on New Advances in Welding and Allied Processes* 2: 3–10.

9. Cullen, T. M., and Freeman, J. W. 1963. Metallurgical factors influencing hot ductility of austenitic piping at weld heat affected zone temperatures. *ASME Journal of Engineering for Power* 85(2): 151–164. DOI: 10.1115/1.3675237

10. Lippold, J. C., and Koteki, D. J. 2005. "Austenitic Stainless Steels." In *Welding Metallurgy and Weldability of Stainless Steels*. Hoboken, N.J.: John Wiley and Sons.

11. Lundin, C. D., et al. 1975. Ferrite-fissuring relationship in austenitic stainless steel weld metals. *Welding Journal* 54(8): 241-s to 246-s.

12. Dhooge, A. 1988. Survey on reheat cracking in austenitic stainless steels and Ni base alloys. *Welding in the World* 41: 206–219.

13. Irvine, K. J., Murray, J. D., and Pickering, F. B. 1960. The effect of heat treatment and microstructure on the high-temperature ductility of 18%Cr-12%Ni-1%Nb steels. *Journal of Iron and Steel Institute*, p. 166–179.

14. Thomas, R. D., and Messler, R. W. 1997. Welding type 347 stainless steel — An interpretive report. *Welding Research Council Bulletin*. Bulletin 421.

15. Kant, R., and DuPont, J. N. 2019. Stress relief cracking susceptibility in high-temperature alloys. *Welding Journal* 98(2): 29-s to 49-s. DOI: 10.29391/2019.98.003

16. Dillingh, E. C. B., and Aulbers, A. P. 2016. Stress relaxation cracking — Augmented recommended practice. TNO2016.

17. van Wortel, H. 2007. Control of relaxation cracking in austenitic high temperature components. Paper read at *NACE Corrosion 2007*, March 2007 in Nashville, Tenn.

18. Dhooge, A., and Vinckier, A. 1987. Reheat cracking — A review of recent studies. *International Journal of Pressure Vessels and Piping* 27: 239–269.

19. Kant, R. 2018. Stress relief cracking susceptibility in high temperature alloys. Master's thesis, Lehigh University.

20. Lippold, J. C. 2014. *Welding Metallurgy and Weldability*. Hoboken, N.J.: John Wiley & Sons. DOI: 10.1002/9781118960332

21. Guan, K., et al. 2005. Effect of aging at 700°C on precipitation and toughness of AISI 321 and AISI 347 austenitic stainless steel welds. *Nuclear Engineering and Design* 235(23): 2485–2494. DOI: 10.1016/j.nucengdes.2005.06.006

22. Ghalambaz, M., et al. 2017. A case study on failure of AISI 347H stabilized stainless steel pipe in a petrochemical plant. *Case Studies in Engineering Failure Analysis* 9: 52–62. DOI: 10.1016/j.csefa.2017.07.001

23. Alpsten, G. A., and Tall, L. 1970. Residual stresses in heavy welded shapes. *Welding Journal* 49(3): 93-s to 105-s.

24. Vickers, N. J. 2017. Animal communication: When I'm calling you, will you answer too? *Current Biology* 27(14): R713–R715. DOI: 10.1016/j.cub.2017.05.064

25. Pang, H., and Pukas, S. 1989. Residual stress measurements in a cruciform welded joint using hole drilling and strain gauges. *Strain* 25(1): 7–14. DOI: 10.1111/j.1475-1305.1989.tb00680.x

26. Prime, M. B. 2001. Cross-sectional mapping of residual stresses by measuring the surface contour after a cut. *Journal of Engineering Materials and Technology* 123(2): 162–168. DOI: 10.1115/1.1345526

27. Chandra, U. 1985. Determination of residual stresses due to girth-butt welds in pipes. *Journal of Pressure Vessel Technology* 107(2): 178–184. DOI: 10.1115/1.3264431

28. Prevéy, P. S. 1996. Current applications of x-ray diffraction residual stress measurement. *Developments in Materials Characterization Technologies*, 103.

29. Owen, R., et al. 2003. Neutron and synchrotron measurements of residual strain in TIG welded aluminium alloy 2024. *Materials Science and Engineering: A* 346(1–2): 159–167. DOI: 10.1016/S0921-5093(02)00547-6

30. Webster, G., and Wimpory, R. 2001. Residual stress in weldments. *Journal of Neutron Research* 9(2–4): 281–287. DOI: 10.1080/10238160108200153

31. Lorentzen, T., and Ibsø, J. 1995. Neutron diffraction measurements of residual strains in offshore welds. *Materials Science and Engineering: A* 197(2): 209–214. DOI: 10.1016/0921-5093(94)09752-6

32. Zhang, W., Feng, Z., and Crooker, P. 2011. Improved procedure for computing residual stresses from neutron diffraction data and its application to multipass dissimilar welds. *Science and Technology of Welding and Joining* 16(3): 254–260. DOI: 10.1179/1362171810Y.0000000023

33. Duquennoy, M., et al. 2001. Ultrasonic characterization of residual stresses in steel rods using a laser line source and piezoelectric transducers. *NDT & E International* 34(5): 355–362. DOI: 10.1016/S0963-8695(00)00075-X

34. Chu, S., Peukert, H., and Schneider, E. 1995. Evaluation of residual stress states in welded plates using ultrasonic techniques. *NDT & E International* 2(28): 120.

35. Ni, J., Zhuang, X., and Abdel Wahab, M. 2020. Review on the prediction of residual stress in welded steel components. *Computers Materials & Continua* 62(2): 495–523. DOI: 10.32604/cmc.2020.08448

36. Mahur, B. P., Bhardwaj, Y., and Bansal, V. 2017. Review on finite element analysis for estimation of residual stresses in welded structures. *Materials Today: Proceedings* 4(9): 10230–10234. DOI: 10.1016/j.matpr.2017.06.354

37. Rong, Y., et al. 2018. Review on finite element analysis of welding deformation and residual stress. *Science and Technology of Welding and Joining* 23(3): 198–208. DOI: 10.1080/13621718.2017.1361673

38. Arora, H., Singh, R., and Brar, G. S. 2019. Thermal and structural modelling of arc welding processes: A literature review. *Measurement and Control* 52(7–8): 955–969. DOI: 10.1177/0020294019857747

39. Marques, E. S., Silva, F. J., and Pereira, A. B. 2020. Comparison of finite element methods in fusion welding processes — A review. *Metals* 10(1): 75. DOI: 10.3390/met10010075

40. Yang, Y. 2021. Recent advances in the prediction of weld residual stress and distortion — Part 1. *Welding Journal* 100(5): 151-s to 170-s. DOI: 10.29391/2021.100.013

41. Wu, X., et al. 2020. Control of weld residual stress in a thin steel plate through low transformation temperature welding consumables. *Welding Journal* 99(4): 124-s to 134-s. DOI: 10.29391/2020.99.012

42. Goldak, J. A., and Akhlaghi, M. 2005. *Computational Welding Mechanics*. New York, N.Y.: Springer Science & Business Media.

43. Nezamdost, M., et al. 2016. Investigation of temperature and residual stresses field of submerged arc welding by finite element method and experiments. *The International Journal of Advanced Manufacturing Technology* 87(1): 615–624. DOI: 10.1007/s00170-016-8509-4

44. Venkatkumar, D., and Ravindran, D. 2016. 3D finite element simulation of temperature distribution, residual stress and distortion on 304 stainless steel plates using GTA welding. *Journal of Mechanical Science and Technology* 30(1): 67–76. DOI: 10.1007/s12206-015-1208-5

45. Joshi, S., et al. 2013. Characterization of material properties and heat source parameters in welding simulation of two overlapping beads on a substrate plate. *Computational Materials Science* 69: 559–565. DOI: 10.1016/j.commatsci.2012.11.029

46. Pickle, T. J., et al. 2021. Effect of PWHT and filler metal on stress relaxation cracking susceptibility in 347H stainless steel welds for elevated temperature service. Master of Science thesis, Colorado School of Mines.

47. AWS D1.6/D1.6M:2017, *Structural Welding Code — Stainless Steel*. Miami, Fla.: American Welding Society.

48. Goldak, J., Chakravarti, A., and Bibby, M. 1984. A new finite element model for welding heat sources. *Metallurgical Transactions B* 15(2): 299–305. DOI: 10.1007/BF02667333

49. Kim, W., et al. 2016. Welding residual stress analysis of 347H austenitic stainless steel boiler tubes using experimental and numerical approaches. *Journal of Mechanical Science and Technology* 30(4): 7. DOI: 10.1007/s12206-016-0333-0

50. Brickstad, B., and Josefson, B. 1998. A parametric study of residual stresses in multi-pass butt-welded stainless steel pipes. *International Journal of Pressure Vessels and Piping* 75(1): 11–25. DOI: 10.1016/S0308-0161(97)00117-8

51. Sawada, K., et al. 2019. Catalog of NIMS creep data sheets. *Science and Technology of Advanced Materials* 20(1): 1131–1149. DOI: 10.1080/14686996.2019.1697616

52. Orzolek, S., DuPont, J., and Siefert, J. 2020. Microstructural evolution of dissimilar metal welds involving grade 91. *Metallurgical and Materials Transactions A* 51(5): 2222–2238. DOI: 10.1007/s11661-020-05715-2

YU HONG, **TIMOTHY PICKLE**, and **ZHENZHEN YU** (*zyu@mines.edu*) are with the Colorado School of Mines, Golden, Colo. **JUDITH VIDAL**, **CHAD AUGUSTINE**, and **YU** are with the National Renewable Energy Laboratory, Golden, Colo.

Rapid Publication of Cutting-Edge Welding Research — *WJRS Letters*

Dear Researchers,

The *Welding Journal Research Supplement* (*WJRS*) is seeking manuscripts for rapid publication of **emerging research that is cutting edge and novel**. The manuscripts are relatively short in length and will be called *WJRS Letters. They are aimed at allowing authors to quickly publish new research results on "hot" topic areas of interest to the WJRS.*

Editor approval is required for submission of *WJRS Letters* manuscripts. If you are interested, please submit an abstract summarizing your proposed manuscript. *WJRS Letters* are not intended to be data dumps or options for publications of low-quality research. Abstracts that do not describe new, cutting-edge research will be declined. If your abstract is accepted, you'll be invited to submit a manuscript. Below are more details.

(1) First, provide an abstract < 500 words, which includes author names, emails, and affiliations, to *wjrs@aws.org*.

A *single figure* (not multipart) with a caption can also be provided with the abstract. **Complete manuscripts submitted without approval will be declined immediately. Do not submit abstracts or manuscripts to the *WJRS* submission website.**

(2) If your abstract is accepted, you'll be invited to write a manuscript of not more than 2200 words with three to four figures (with captions). You will receive a template for your *Letters* after abstract approval; visit *aws.org/library/doclib/WJRS-guidelines.pdf*. All content must fit into **five** pages when laid out in the current *WJRS* format reflected in the template. Manuscript content must fit into the template without format changes to be published.

(3) Manuscripts will require succinct, focused communication with the following sections:

- **Introduction/Background/Objectives**
- **Procedures**
- **Results**
- **Discussion**
- **Conclusions**
- **Limited References**

If you have questions, please email *wjrs@aws.org*. Thank you for supporting this effort.

Sincerely,

Thomas J. Lienert, PhD, FASM, FAWS
Review Editor

American Welding Society